

The Earth as an extrasolar transiting planet

Earth's atmospheric composition and thickness revealed by Lunar eclipse observations^{*}

A. Vidal-Madjar¹, L. Arnold², D. Ehrenreich³, R. Ferlet¹, A. Lecavelier des Etangs¹, F. Bouchy^{1,2}, D. Segransan⁴, I. Boisse¹, G. Hébrard¹, C. Moutou⁵, J.-M. Désert^{1,6}, D. K. Sing^{1,7}, R. Cabanac⁸, C. Nitschelm⁹, X. Bonfils³, X. Delfosse³, M. Desort³, R. F. Diaz¹, A. Eggenberger³, T. Forveille³, A.-M. Lagrange³, C. Lovis⁴, F. Pepe⁴, C. Perrier³, F. Pont⁷, N. C. Santos^{4,10}, and S. Udry⁴

¹ Institut d'Astrophysique de Paris, UMR7095 CNRS, Université Pierre & Marie Curie, 98bis, boulevard Arago, 75014 Paris, France, e-mail: alfred@iap.fr

² Observatoire de Haute-Provence, CNRS/OAMP, 04870 Saint-Michel-l'Observatoire, France

³ Laboratoire d'Astrophysique de Grenoble, Université Joseph Fourier, CNRS (UMR 5571), BP 53, 38041 Grenoble cedex 9, France

⁴ Observatoire de Genève, Université de Genève, 51 Chemin des Maillettes, 1290 Sauverny, Switzerland

⁵ Laboratoire d'Astrophysique de Marseille, Université de Provence, CNRS (UMR6110), BP 8, Technopôle Marseille Étoile, 13376 Marseille Cedex 12, France

⁶ Harvard-Smithsonian Center for Astrophysics, 60 Garden Street, Cambridge, Massachusetts 02138 USA

⁷ School of Physics, University of Exeter, Exeter, EX4 4QL, UK

⁸ Observatoire Midi-Pyrénées, TBL, 57 Ave d'Azereix, 65000 Tarbes, France

⁹ Instituto de Astronomía, Universidad Católica del Norte, Avenida Angamos 0610, Antofagasta, Chile

¹⁰ Centro de Astrofísica, Universidade do Porto, Rua das Estrelas, 4150-762 Porto, Portugal

Abstract

Context. An important goal within the quest for detecting an Earth-like extrasolar planet, will be to identify atmospheric gaseous bio-signatures.

Aims. Observations of the light transmitted through the Earth's atmosphere, as for an extrasolar planet, will be the first important step for future comparisons. We have completed observations of the Earth during a lunar eclipse, a unique situation similar to that of a transiting planet. We aim at showing what species could be detected in its atmosphere at optical wavelengths, where a lot of photons are available in the masked stellar light.

Methods. We present observations of the 2008 August 16 Moon eclipse performed with the SOPHIE spectrograph at the Observatoire de Haute-Provence (France). Locating the spectrograph's fibers in the penumbra of the eclipse, the Moon irradiance is then a mix of direct, unabsorbed Sun light and solar light that has passed through the Earth's atmosphere. This mixture essentially reproduces what is recorded during the transit of an extrasolar planet.

Results. We report here the clear detection of several Earth atmospheric compounds in the transmission spectra, such as ozone, molecular oxygen, and neutral sodium as well as molecular nitrogen and oxygen through the Rayleigh signature. Moreover, we present a method that allows us to derive the thickness of the atmosphere versus the wavelength for penumbra eclipse observations. We quantitatively evaluate the altitude at which the atmosphere becomes transparent for important species like molecular oxygen and ozone, two species thought to be tightly linked to the presence of life.

Conclusions. The molecular detections presented here are an encouraging first attempt, necessary to better prepare for the future of extremely-large telescopes and transiting Earth-like planets. Instruments like SOPHIE will be mandatory when characterizing the atmospheres of transiting Earth-like planets from the ground and searching for bio-marker signatures.

Key words. Planets and planetary systems - Eclipses - Earth - Planets and satellites: atmospheres - Astrobiology - Techniques: spectroscopic - Methods: observational

1. Introduction

Soon the *CoRoT* (a space program operated by the French Space Agency, CNES) and *Kepler* (a NASA spacecraft searching for habitable planets) missions may discover a transiting Earth-like planet. It will then be of prime importance to study such an exoplanet's atmospheric composition, in order to define its evolutionary

status as compared to the known Earth one. Through these observations the impact of galactic environmental perturbations as, e.g. the passing through a dense interstellar cloud (Vidal-Madjar et al. 1978), may be directly evaluated. However, the ultimate goal of these studies will be to know if life could have emerged elsewhere as it did once on Earth.

It has been demonstrated, as for the exoplanet HD209458b, that it is possible to detect the presence of some species in the planetary atmosphere, like sodium, hydrogen, oxygen, and carbon (Charbonneau et al. 2002, Vidal-Madjar et al. 2003, 2004). More recently, additional detections have been re-

* Detailed observations as shown in Figs. 9, 10, 11 and 12 are only available in electronic form at the CDS via anonymous ftp to cdsarc.u-strasbg.fr (130.79.128.5) or via <http://cdsweb.u-strasbg.fr/cgi-bin/qcat?J/A+A/>

ported, including HI from recombination via the Balmer jump (Ballester et al. 2007), H₂ the main gaseous content via Rayleigh scattering (Sing et al. 2008a, 2008b, Lecavelier des Etangs et al. 2008b), and TiO/VO (Désert et al. 2008). The possible signature from H₂O in HD209458b (Barman 2007) is now strongly questioned by new *HST* (the Hubble Space Telescope) and *Spitzer* (a Space Telescope, studying the universe in infrared) observations, revealing on the contrary the presence of high-altitude haze as well as CO in the atmosphere of HD189733b (Ehrenreich et al. 2007, Lecavelier des Etangs et al. 2008a, Sing et al. 2009, Désert et al. 2009). New transiting planets are discovered from space by *CoRoT*, launched at the end of 2006, and by *Kepler* launched in March 2009. More specifically, space observations are reaching high enough accuracy to enable the detection of Earth-size transiting planets (Bordé et al. 2003, Rouan et al. 2009, Léger et al. 2009, Queloz et al. 2009), some of which are possibly “ocean-planets” (Léger et al. 2004) or even similar to the telluric planets of our Solar System, at distances compatible with a so-called habitable zone. Obviously, the characterization of the corresponding atmospheres would be an exciting achievement.

Knowing that the probability to have a transiting Earth at about one AU from its star is of the order of 0.5%, and that the number of available planets rises as the cube of their distance from the Sun, Ehrenreich et al. (2006) have shown that the number of available transiting planets within 60 pc is similar to the number of possible targets available if one looks at the planetary emissions within a sphere of about 10 pc around the Sun (the current expectations of projects like *TPF-I* (the NASA, Terrestrial Planet Finder via Interferometry) or *Darwin* (the ESA equivalent program)). However, the present difficulty of the transiting approach is the lack of photons (*i.e.* high S/N) necessary to analyze spectra of Earth-like planets when using 2-m class telescopes. Lecavelier des Etangs & Ehrenreich (2005) have shown that many hot Jupiters, hot Neptunes, ocean planets, and other low-density planets will be observable with larger ground based telescopes, like the future European Extremely-Large Telescope (E-ELT). Transmission spectroscopy has already proved its potential to probe atmospheres of extrasolar planets. It could very well be the first method which will give access to the atmosphere of smaller and cooler transiting planets, hopefully Earth-like.

Observing in the visible and near UV offers a great advantage, because of the strong opacity of some specific narrow line species in that spectral range, and because of the often more intense stellar flux at these wavelengths. During a transit event, only the upper atmosphere of the planet may be seen, thus reducing the many perturbing effects potentially present when observing at lower resolution, *i.e.* at lower altitudes, like the presence of clouds, continents, oceans etc. as shown in Arnold et al. 2002, Woolf et al. 2002, Arnold 2008 and references therein. Indeed, in the core of the spectral lines we will sample only the upper atmosphere, where one can expect that the mixing of different species has already taken place, thus revealing an “average” planetary atmosphere representative of overall signatures.

Following the pioneering work of Sagan et al. (1993) searching for “life on Earth” from remote sensing, our purpose is to observe the Earth as a transiting planet in order to better test the present models of Earth-like planets and thus get ready to properly analyze future observations of real transiting Earth-like extrasolar planets. Using the Moon as a reflective surface during total or partial eclipses provides the needed situation which furthermore can be exploited from the ground. We have conducted a first attempt during the 2008 August 16

lunar eclipse with the SOPHIE high-resolution spectrograph (Perruchot et al. 2008, Bouchy et al. 2009) at the 1.93 m telescope of the OHP (Observatoire de Haute Provence) observatory covering the 3 900 to 7 000 Å spectral range at a resolving power of $R \sim 75\,000$. The choice of a high-resolution spectrograph allows us to better identify absorbing species via their detailed spectral signatures.

Other observations of this eclipse have been conducted (Pallé et al. 2009) over a wider wavelength range (0.36 - 2.4 μm), but at a lower spectral resolution ($R < 1\,000$), resulting in a mainly qualitative identification of the Earth’s atmospheric compounds. Here, we will focus on quantitative results. In Sect. 2, the SOPHIE observations are described, then a quantitative data analysis is given in Sect. 3, followed by a direct comparison with current model predictions in Sect. 4. We show that indeed, in the visible range some of the main Earth’s atmospheric compounds are identified and evaluated.

2. Observations

The observations were conducted with the cross-dispersed, environmentally stabilized echelle spectrograph SOPHIE, dedicated to high-precision radial velocity measurements (Perruchot et al. 2008, Bouchy et al. 2009). They were secured in *high-resolution* mode, *i.e.* the spectrograph was fed by a 40 μm slit and an optical scrambler located at the output of the optical fiber, allowing a resolving power $\lambda/\Delta\lambda = 75\,000$.

Two optical fibers, 3 arcsec wide, separated by 1.86 arcmin were used. Both were placed on the Moon and aligned along the east-west direction.

The spectra were extracted from the detector images with the SOPHIE pipeline, which includes localization of the orders on the 2D-images, optimal order extraction, cosmic-ray rejection, wavelength calibration, corrections of flat-field and charge transfer inefficiency at low signal-to-noise ratio (Bouchy et al. 2009).

2.1. Fibers position on the Moon

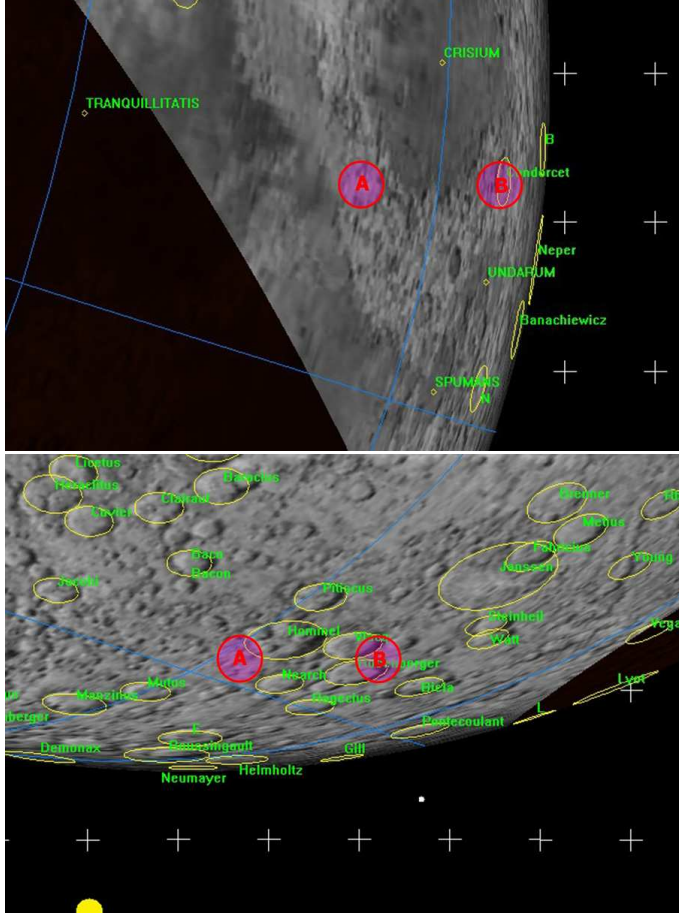
Table 1 lists the three main spectra used in our analysis along with their positions over the Lunar disk as shown in Fig. 1. Only one observation during the eclipse was useful, taken at 20h44 UT in the penumbra, close to the Earth shadow. Figure 1 shows where the fibers were positioned, *i.e.* over high-albedo Imbrium-type or pre-Imbrium-type terrains (for more information see the URL at the end of the reference list), which maximized the flux during the eclipse. The two other observations listed in Table 1 are two among a total of 13 calibration spectra recorded after the eclipse (full Moon outside the penumbra) at similar air masses ($\sec(z)$ in Table 1 where z is the zenith angle) and over the two different regions pointed to during the eclipse. Unfortunately, after the eclipse the guiding camera was saturated and an accurate position of the fibers could not be checked and adjusted visually as during the eclipse. Nevertheless the telescope coordinates indicate that the fibers were positioned over the same kind of lunar terrains.

2.2. Observations log

We collected only sparse observations, because clouds appeared just after the first exposure taken at 20h44 UT. These clouds disappeared for a few minutes at 22h44 UT, just before the umbra left the Moon, though these observations are more noisy and are still possibly affected by intervening clouds.

Table 1. Fibers positions on the Moon during and after the eclipse. Times are for mid-exposure.

Date; Time (UT)	Fiber A location longitude; latitude	Fiber B location longitude; latitude	Exposure time (s)	BERV (km/s)	Air mass $sec(z)$
2008-08-16; 20:44:21	E 52.0°; N 9.8°	E 68.5°; N 12.1°	198.92	-0.064	2.94
2008-08-17; 00:11:56	E 39°; S 51°	E 50°; S 48°	2.00	-0.408	1.86
2008-08-17; 02:55:45	E 47°; N 20°	E 64°; N 22°	3.00	-0.667	2.99

**Figure 1.** Fibers A and B on the Moon in penumbra. The umbra is the dark area at the left (upper figure at 20h44 UT) and at right (lower figure at 22h44 UT). The distance between the fibers is 1.86 arcmin, east-west oriented.

The observations completed at 20h44 UT were done with fibers A and B at about 2 and 4 arcmin from the penumbra/umbra limit respectively.

Spectra were also taken later in the night after the eclipse, when the clouds moved away. In particular at 02h56 UT spectra were taken over the same location on the Moon and at the same air mass as those at 20h44 UT. The spectrum taken at 00h12 UT, although pointed over another region of the Moon, is also listed because it was taken with a shorter time gap from the 20h44 UT eclipse observation, leading to a smaller differential BERV correction (“Barycentric Earth Radial Velocity” correction of the Earth’s motion along its orbit to evaluate the spectral observations in heliocentric coordinates as automatically done through the SOPHIE pipeline). The corresponding BERV shifts are also listed in Table 1.

The calibration spectra (taken later in the night after the eclipse) are used to correct the eclipse spectra from the direct at-

mospheric absorption along the line of sight between the Moon and the OHP Observatory and to extract the altitude at which the Earth atmosphere becomes transparent enough for a grazing line of sight.

3. Data analysis

Because we are searching for atmospheric signatures in the gathered spectra, we have first to recalculate the wavelengths in the geocentric reference frame. We know that there all atmospheric signatures will be present at identical wavelengths, while the solar line signatures will be slightly displaced by an amount related to the spectral shift induced by the BERV. Note however that at the SOPHIE resolution of about ~ 4 km/s, these shifts of less than 0.5 km/s are likely insignificant. The possible impact of the BERV effect on our data is assessed in Sect. 5.

Our observations present two types of Earth atmospheric absorption signatures : i) the “vertical” ones produced along the path length between the Moon and the telescope and ii) the “horizontal” ones due to the solar light grazing the Earth atmosphere before reaching the Moon. We are only interested in the latter and will therefore have to correct the data from the “vertical” signatures.

Finally, knowing that the SOPHIE pipeline is optimized for high radial velocity precisions and not for flux evaluations, we can expect some difficulties related to flux estimates, *i.e.* echelle order corrections as well as precise zero level evaluations.

3.1. The “vertical” Earth atmospheric transmission function

The “vertical” atmospheric transmission is a function that depends upon the air mass AM , noted $T_{AM}(\lambda)$. Along the line of sight, an initial spectrum $I(\lambda)$ reaching the top of the atmosphere is transformed into an observed spectrum $O_{AM}(\lambda)$:

$$O_{AM}(\lambda) = I(\lambda) \times T_{AM}(\lambda). \quad (1)$$

For a plane parallel atmosphere (an approximation valid to air masses smaller than ~ 5) the air mass AM is equal to $a = sec(z)$ and the atmospheric transmission function is then simply $T^a(\lambda)$, the transmission function T at the power a (Bird et al. 1982), where T is the transmission in the vertical direction (air mass of 1).

Indeed for an air mass a equal to the sum of two air masses a_1 and a_2 , one can evaluate the observed spectrum in the following manner :

$$O_{a_1+a_2} = I \times T^{a_1+a_2} = (I \times T^{a_1}) \times T^{a_2}, \quad (2)$$

showing that the transmission function $T(\lambda)$ follows the conditions :

$$T^{a_1+a_2}(\lambda) = T^{a_1}(\lambda) \times T^{a_2}(\lambda) \quad (3)$$

and

$$T^0(\lambda) = 1. \quad (4)$$

If the transmission function $T(\lambda)$ is known at a given air mass, it can be evaluated at any other air mass. Noting that

$$\frac{O_{a_1}(\lambda)}{O_{a_2}(\lambda)} = \frac{T^{a_1}(\lambda)}{T^{a_2}(\lambda)} = T^{a_1-a_2}(\lambda), \quad (5)$$

we were able to evaluate directly the transmission function at different air masses through the complete series of spectra gathered during the full Moon observations. We normalized all evaluations extracted from observational ratios to an air mass equal to 1 by calculating

$$\left(\frac{O_{a_1}(\lambda)}{O_{a_2}(\lambda)}\right)^{1/(a_1-a_2)} = (T^{a_1-a_2}(\lambda))^{1/(a_1-a_2)} = T(\lambda). \quad (6)$$

From the 13 full Moon observations $O_a(\lambda)$, we extracted 24 couples well separated in air mass each containing independent evaluations of the transmission function $T(\lambda)$. In Fig. 2, the average of all evaluations are shown, providing the reference transmission function $T(\lambda)$ that we will now use in the following data analysis to re-evaluate all observed eclipse spectra as if they were observed from outside the atmosphere.

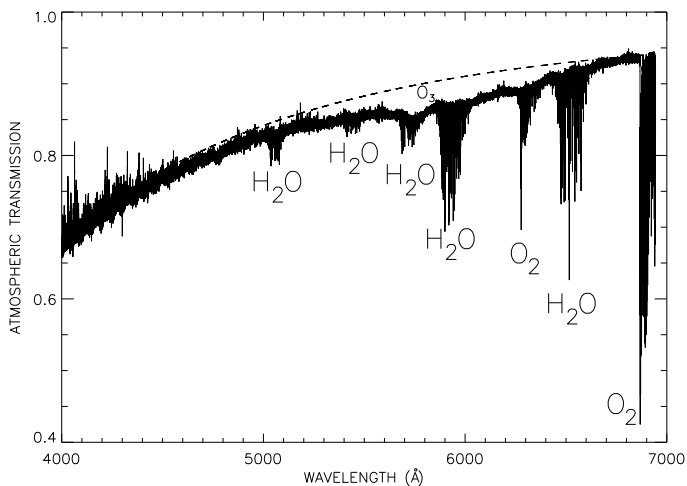


Figure 2. Average atmospheric transmission function $T(\lambda)$ as evaluated during full Moon just after the eclipse supposed to be similar to the one during the eclipse observations. The dashed line shows a transmission model (Hayes and Latham 1975), which includes both Rayleigh diffusion and aerosols (optical depth of 0.035 at 5320 Å typical for clear OHP nights). The experimental evaluation was normalized in order to match the model at our reference wavelength $\lambda_0 = 4530$ Å (see Sect. 5). O_2 as well as H_2O absorption bands are clearly seen. Note that the match with the model is good except for the central region from 5000 to 6700 Å, where a clear additional absorption is detected. This is the Chappuis band from ozone (noted O_3), not included in the model calculation.

3.2. Other corrections of the SOPHIE spectra

One can note in Fig. 2 the SOPHIE echelle order signatures as regular wiggles over ~ 80 Å from 4000 to 4500 Å, where they are particularly visible. Those instrumental signatures should not be seen in an atmospheric transmission function. These will certainly be a perturbation in our data analysis, but for the time

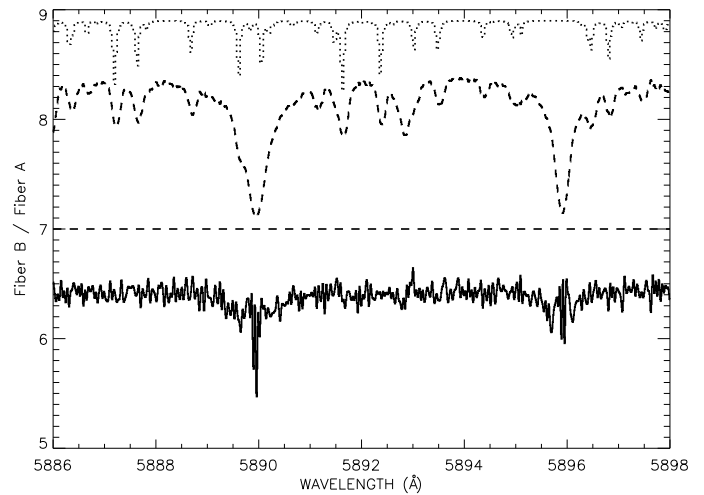


Figure 3. At 20h44 UT, the (Fiber B / Fiber A) ratio (solid line) is shown in the NaI doublet spectral region. The Fiber A spectrum (dashed line) with its corresponding zero level (horizontal dashed line) as extracted from the SOPHIE pipeline as well as an H_2O model (dotted line) are overplotted (in arbitrary scales simply to fit within the figure frame) to show the positions of the solar as well as H_2O spectral lines in the spectrum. Most of the observed lines are due to atmospheric water vapor. They disappear in the fiber's spectral ratio, while the broad spectral wings of the two NaI solar lines are still clearly visible.

being we will try to analyze the data without a modification to the SOPHIE pipeline. We will however evaluate the impact of this approximation a posteriori by looking how these order signatures are affecting the results (see Sect. 5).

In Fig. 3, both the direct Fiber A spectrum observed during the eclipse as well as the Fiber B/Fiber A flux ratio are shown close to the NaI doublet solar lines. Note that the numerous spectral lines, mostly due to H_2O in the Earth atmosphere, completely disappear from the Fiber B/Fiber A ratio. This is not surprising because both Fibers A and B are observed through the same atmospheric (and thus air mass) layer.

Although most of the weaker solar lines are also erased in this ratio (as it can be directly seen in Fig. 2, which also shows spectral ratios, see Eq. 6), for strong and deep solar lines like *e.g.* the NaI lines, as shown in Fig. 3, the signature of their broad spectral wings is still visible in the Fiber B/Fiber A ratio. This should not be the case if Fiber A and B have simply a different transmission coefficients, because they are both simultaneously observing (almost) the same solar spectrum.

The NaI lines (reaching close to the zero level, see Fig. 3) are more sensitive to any unaccounted for, even small, zero level shift. This is not the case for the weaker solar lines.

Knowing that a zero level shift is present in the extracted spectra, we search below for some plausible explanations.

3.2.1. An instrumental zero level shift

Over the SOPHIE CCDs, the lowest counts are not equal to zero (even where no counts should be registered), as for instance at the shortest wavelengths, where the instrument sensitivity drops sharply. For this reason, we assumed the possibility of a zero offset in the SOPHIE extracted counts. We thus subtracted a value from the SOPHIE spectra to make the broad NaI solar lines wings disappear (as they should). This correction is compatible with the data, as reported in Table 2.

Table 2. SOPHIE fluxes as extracted from the data sets, both at the minimum of deep absorption signatures and where the flux is maximum. Times are for mid-exposures. Flux units are arbitrary but comparable in relative terms because they correspond to the raw data (CCD ADU) corrected for by the same pipe line.

Fiber ; time (UT)	Min. flux in NaI	Min. flux in O ₂	Max. flux
A ; 20:44	0.0007	0.0005	0.0205
B ; 20:44	0.004	0.002	0.106
A ; 02:56	0.0018	0.0010	0.0514
B ; 02:56	0.0016	0.0008	0.0471

We tried three zero shift level scenarios :

1. we assumed that stray light due to the nearby full Moon is present. However, subtracting various proportions of the full moon spectrum to the other spectra did not induce any attenuation of the NaI solar wings and on the contrary produced many additional solar lines;
2. we supposed that a constant value has to be subtracted from all data, proportional to the total flux gathered in each spectrum. Again no satisfactory solution was found;
3. we assumed that a unique constant value had to be used for all spectra, a correction only related to the detector and independent of the total flux. Then we found that by subtracting 0.0003 ± 0.0001 from all SOPHIE extracted values, it was possible to completely wash out the NaI solar wings. This 0.0003 value represents a maximum relative continuum correction of 14% in the blue, decreasing to 1.5% in the red, for the fiber A spectrum. For fiber B, which is brighter, the relative continuum correction is one order of magnitude lower.

We verified that this last correction (3.) was also adapted at the end of our study, because no broad wing solar NaI lines signatures should show up in any information related uniquely to the Earth's atmosphere. The corresponding final result (with and without this correction) is shown in Sect. 5, Fig. 10.

This simple third correction (3.) does not seem to be wavelength-dependent, because as we show in Table 2, at the wavelengths of the very deep O₂ absorption lines near 6900 Å, it is clear that this correction could not be larger than the minimum flux seen at the bottom of the absorption lines, and thus has to be somewhere in the 0 to 0.0005 range, which we found to be the case. A posteriori, we will also see that the final results are all compatible with this correction.

After empirically evaluating the type of correction needed, we found that another possible explanation of atmospheric origin may be given and we develop it in the next section.

3.2.2. An astrophysical zero level shift : the ring effect

Indeed, following a suggestion of our referee, we recalled that some of the sunlight going through the Earth atmosphere is refracted in the lower layers of the atmosphere, producing for an observer on the Moon within the Earth umbra, an emission ring all along the Earth limb.

This ring effect can contribute here in two ways. First, it can add a constant intensity (a few percent shift of the zero level) to sunlight as seen in scattered light from the sky, to the extent that the penumbral light contains not just transmitted light, but also forward-scattered light ; this should slightly dilute the penumbral spectrum and introduce a zero level correction of type

(2). Second, the light reflected from the lunar surface itself will contain the ring effect, again a few percent additive background spectrum, a correction of type (2.) or (3.).

The ring relative intensity and spectral signature were already observed during Lunar eclipses through the study of the lunar light reflected from the umbral regions, only lit by the Earth ring. Danjon (1936) very early understood that the umbral luminosity was related to the transparency of the Earth lower atmosphere and after observing several lunar eclipses, he proposed a related five level scale for the lunar umbral luminosity.

Observation revealed (as in *e.g.* Hernitschek et al. 2008) that a 5 magnitudes drop exists at the penumbra-umbra (PU) transition, showing that the ring contribution to the penumbral flux is on the order of 1 %. Furthermore, the ring contribution decreases when moving away from the PU transition deeper within the umbra, as the expected signature of forward-scattered light. The ring contribution within the penumbral region is indeed proportional to the length of the Earth's limb (L_E) just in front of the solar disk appearing on top of the Earth limb.

Thus, when moving in the penumbral domain away from the PU transition, the direct solar contribution increases like the surface of the solar disk above the Earth limb ($\sim L_E^2$, see Fig. 4), while the ring contribution increases as the length of the Earth's limb covered by the solar disk ($\sim L_E$). This means that for our observations, the *relative* ring effect contribution should be stronger in Fiber A than in Fiber B according to the geometry of our 20h44 UT observation, for which Fiber A, presenting a lower signal, is closer to the PU transition than Fiber B. The ring effect contribution in the reflected Lunar light seems thus to better correspond to our empirical correction scenario (3.).

This is confirmed in the Gedzelman & Vollmer (2008) simulation of irradiance of lunar eclipses. They furthermore show that the ring contribution at the PU transition should present an almost flat spectral signature from 4000 to 7000 Å (see their Fig. 1), *i.e.* over the whole SOPHIE spectral range. This was directly observed during the 2008 August 16 lunar eclipse by Pallé et al (2009, see top of their Fig. S3 of the supplementary section), who detected only weak spectral signatures deeper in the umbra as also predicted by Gedzelman & Vollmer (2008).

In summary the ring contribution should be on the order of 1 % of the signal in Fiber A, and be at a relatively lower level in Fiber B with no wavelength dependence. This is almost exactly what we have found from our empirical study (3.), which presents the same 0.0003 zero level shift in both Fibers, *i.e.* indeed on the order of 1 % in Fiber A and relatively less in Fiber B (see Table 2). Additional discussions in Sect. 5 will show that this correction is on the same order near the NaI doublet lines at 5900 Å and near the molecular O₂ lines at 6900 Å and thus is indeed weakly variable with wavelength.

The ring effect could also explain why the ratios (Eclipse A)/(Full Moon A), (or B) could also be affected, ratios that we are going to use and describe in the following sections.

Both these instrumental and ring effects are probably present in our study and need to be corrected for empirically. In future studies we will also try to observe umbral spectra in order to have a more quantitative evaluation of the ring effect and thus include its contribution in our analysis.

4. Quantitative analysis

We present in this section the approach developed to extract a quantitative information from the observed spectra related to the altitude at which the Earth atmosphere becomes transparent as a

function of wavelength, a result very similar to the one obtained for a transiting planet.

4.1. Determination of the unabsorbed full Moon and eclipse spectra

These unabsorbed spectra are simply recomputed by dividing the observed spectra $O_a(\lambda)$ by the transmission function $T(\lambda)$ at the power of the precise air mass of the corresponding observation :

$$I(\lambda) = O_a(\lambda)/T^a(\lambda). \quad (7)$$

All these calculated corrected spectra are those an observer should have obtained from above the Earth atmosphere. We will note these spectra $E(\lambda)$ and $F(\lambda)$, corresponding to the ‘‘eclipse’’ and ‘‘full Moon’’ corrected spectra respectively.

4.2. Earth’s atmosphere effective thickness

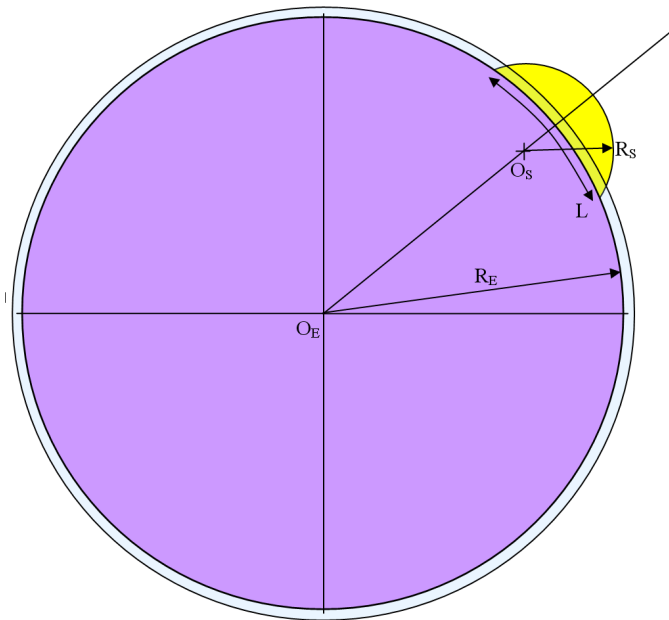


Figure 4. Geometry of a crescent of Sun, S , above the Earth’s reference limb (O_S and R_S are the center and radius of the Sun, O_E and R_E those of the Earth). The scene (not to scale) is observed from the Moon at the location where are positioned fibers A or B within the penumbra. From the observational knowledge of S_A or S_B as extracted from Eq. 11 (see text), the entire defined geometry of the observations allows a direct evaluation of the corresponding arc lengths, L_A or L_B .

From the deep penumbra, where the spectrograph’s fibers are located during the observation, a crescent of Sun is seen above the Earth’s limb. The Moon irradiance is thus a mix of direct Sun light (i.e. unaffected by the Earth’s atmosphere), and solar light that passed through the atmosphere, mostly along an arc L where the solar disk intersects the Earth’s limb (Fig. 4). This mix of direct and absorbed solar light essentially reproduces what is recorded during a transit. Let us note S_\odot as the surface of the full solar disk, S the fraction of solar surface visible above Earth’s geometrical limb during the eclipse, and h is an equivalent height over which the atmosphere can be considered opaque, at each

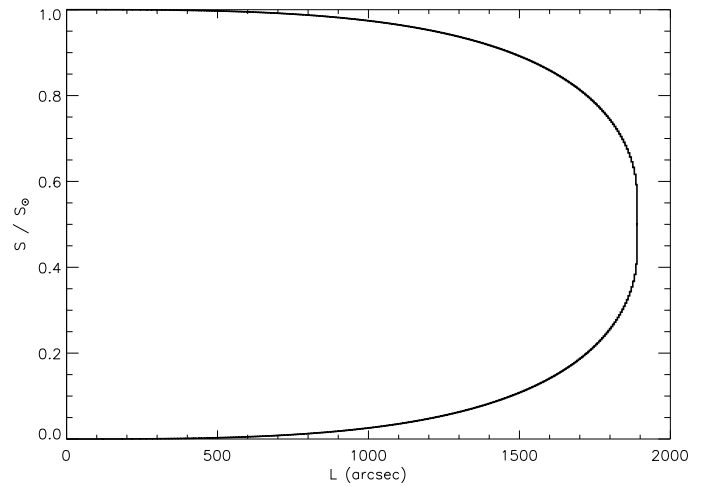


Figure 5. $L = f(S)$ function computed here for the geometry of the eclipse: S is the surface of the solar crescent above the Earth’s reference limb - as observed from the Moon at the location of either fiber A or B within the penumbra. From there, the diameters of the Earth and the Sun are 6 768.0 and 1 890.6 arcsec respectively. This geometry implies the relation shown between the length of the Earth’s limb covered by the Sun L , and the surface of the solar crescent, normalized to the total solar disk surface S_\odot as seen from the Moon. Since S_A/S_\odot or S_B/S_\odot are known from observations, the corresponding arcs lengths L_A or L_B are also known, and thus $h(\lambda)$ evaluated.

wavelength, from the point of view of the geometrical cross section.

The total column density along a grazing line of sight passing through the terminator at different altitudes could be estimated following the Fortney et al. (2005) formulation: the optical depth, τ , in a line of sight grazing the Earth limb at an altitude h is given by

$$\tau(\lambda, h) \approx \sigma(\lambda)n(h) \sqrt{2\pi R_E H}, \quad (8)$$

where R_E is the Earth radius, H the atmosphere scale height, and $n(h) = n_{(h=0)} \exp(-h/H)$ the volume density at the altitude h of the main absorbent with a cross section $\sigma(\lambda)$. The scale height is given by the relation $H = kT/\mu g$, where k is the Boltzmann constant, T the temperature, μ the mean mass of atmospheric molecules times the mass of the proton, and g the gravity at the Earth radius, $g = M_E G/R_E^2$ with M_E equal to the Earth mass and G the gravitational constant.

For any wavelength, the line of sight becomes opaque at an effective altitude h for an effective optical thickness of $\tau_{eff} = 0.56$ as demonstrated to be appropriate for most atmospheric conditions by Lecavelier des Etangs et al. (2008a). We will then be able to compare our equivalent effective altitude h as a function of wavelength to model calculations of effective altitudes.

The effective altitude of the atmosphere at a wavelength λ is calculated by solving the equation $\tau(\lambda, h) = \tau_{eff}$. Using the quantities defined above, the effective altitude h is given by Eq.9.

$$h(\lambda) = H \ln \left((n_{(h=0)} \sigma(\lambda) / \tau_{eff}) \sqrt{2\pi R_E / kT \mu g} \right). \quad (9)$$

In principle, a simple relation links the two $E(\lambda)$ and $F(\lambda)$ corrected spectra due to the geometry of the problem

$$E(\lambda) = F(\lambda) \times \frac{S - L \times h(\lambda)}{S_\odot}. \quad (10)$$

4.3. Evaluation of $h(\lambda)$, the effective height of the Earth atmosphere.

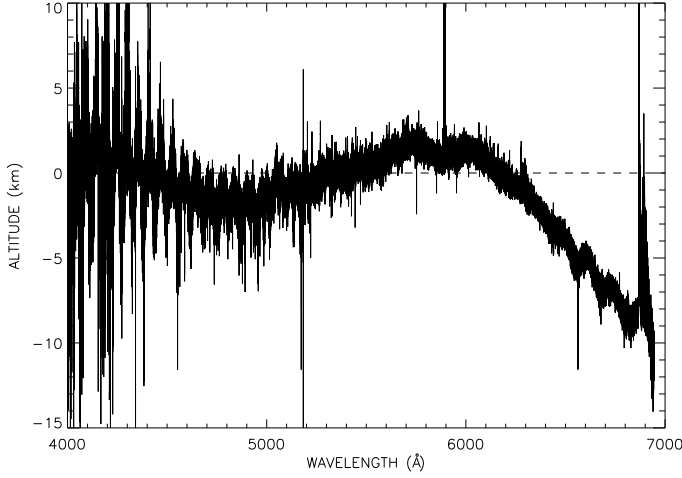


Figure 6. Absorbing atmosphere thickness versus wavelength, evaluated according to Eq. 14 for the 20h44 UT eclipse observation associated to the 02h56 UT full Moon ones. The reference altitude equal to 0 km (dashed line) has been chosen for $\lambda = 4530 \text{ \AA}$. The profile is dominated by the Chappuis band of ozone from 4800 to 6900 \AA , while some signatures due to sodium and oxygen show up near 5890 \AA and 6900 \AA respectively. In the blue region (4000 to 4800 \AA), the Rayleigh scattering is clearly seen. Across that region, the signal drops and produces more noise over the extracted altitudes, also revealing there that the SOPHIE orders are not fully corrected. This is also true longward from about 6500 \AA .

We can define a reference altitude $h(\lambda_0) = 0$ at an arbitrary wavelength λ_0 . Then, S is more precisely the fraction of solar surface visible above the Earth’s limb corresponding to our reference altitude $h(\lambda_0)$. It follows that Eq. 10 reduces to

$$E(\lambda_0) = F(\lambda_0) \times \frac{S}{S_\odot}. \quad (11)$$

The S/S_\odot ratio can be geometrically calculated for a given observation time, but may also be directly estimated from the $E(\lambda_0)$ and $F(\lambda_0)$ values of the flux measured during and outside the eclipse at λ_0 . We decided to take the reference wavelength over a 20 \AA range centered at $\lambda_0 = 4530 \text{ \AA}$, where the absorption in the Earth atmosphere (see Fig. 2) is mainly due to Rayleigh scattering. Because the altitude above sea level (corresponding to the same reference wavelength) is the standard outcome from any atmospheric model calculation (see next section), it will be then simple to shift all our evaluated altitudes relative to our reference altitude $h(\lambda_0)$ into “real” altitudes, above sea level. Indeed all our altitude evaluations $h(\lambda)$ relative to $h(\lambda_0)$, could be positive or negative depending on more or less absorption at λ than at λ_0 .

The ratio of Eqs. 10 and 11 gives for Fiber A

$$\frac{E_A(\lambda)}{E_A(\lambda_0)} = \frac{F_A(\lambda)}{F_A(\lambda_0)} \times \left[1 - \frac{L_A}{S_A} \times h(\lambda)\right], \quad (12)$$

and for Fiber B

$$\frac{E_B(\lambda)}{E_B(\lambda_0)} = \frac{F_B(\lambda)}{F_B(\lambda_0)} \times \left[1 - \frac{L_B}{S_B} \times h(\lambda)\right], \quad (13)$$

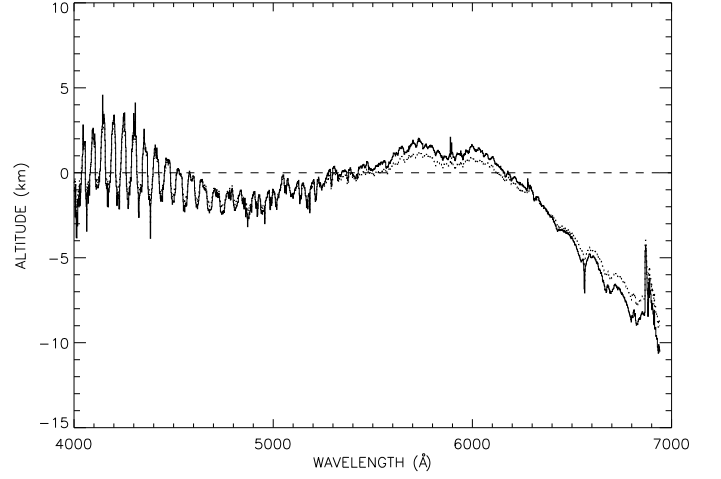


Figure 7. Same as Fig. 6, but here the $h(\lambda)$ variations are binned over 200 pixels ($\sim 2 \text{ \AA}$) for clarity. Here the altitude variations are, following Eq. 14, extracted from the eclipse observations of 20h44 UT with either the 02h56 UT (solid line) or the 00h12 UT (dotted line) full Moon ones. Without the binning the difference was not visible. Here we can note that both possible perturbations related to either the BERV shift as well as the air mass correction are indeed negligible (see text). On the contrary some broadband variations could be seen, probably linked to albedo variations of the different lunar regions where the fibers were pointed (see Table 1). In the blue region (4000 to 5000 \AA), the fringes are due to an imperfect correction of the SOPHIE orders and not to classical CCD interfringe fringes (see text).

in which L_A and L_B are the lengths of the arc of limb at the $h(\lambda_0)$ level as seen from the locations of Fiber A and Fiber B respectively, as projected on the Moon, and similarly S_A and S_B are the corresponding surfaces of the Sun above these Earth’s limbs.

The difference between the ratios for Fibers A and B, (Eq. 12 – Eq. 13), is

$$\begin{aligned} \left(\frac{E_A(\lambda)}{E_A(\lambda_0)} \times \frac{F_A(\lambda_0)}{F_A(\lambda)} - \frac{E_B(\lambda)}{E_B(\lambda_0)} \times \frac{F_B(\lambda_0)}{F_B(\lambda)} \right) &= \\ &= \left(\frac{L_B}{S_B} - \frac{L_A}{S_A} \right) \times h(\lambda). \end{aligned} \quad (14)$$

Therefore, the measurements (left side of Eq. 14) are proportional to h .

However, to fully solve the problem, one needs to evaluate the factor of proportionality in front of h . We know the relative angular diameters of both the Earth (above the Earth’s reference limb) and the Sun, as seen from the Moon at the time of the observations, which unambiguously defines (geometrically) how far above that selected Earth’s limb reference the solar disc emerges. From a simple geometrical calculation (see Fig. 4), one can evaluate the corresponding arc lengths L_A and L_B , which are directly derived from the relation $L = f(S)$ that we have calculated for the time of the observations, as shown in Fig. 5. Finally, the direct measurements of S_A and S_B are extracted from the observations through Eq. 11.

For example, from our best observations made on August 16 at 20h44 UT during the eclipse, compared to the full Moon observations made on August 17 at 02h56 UT, we find the following corrected flux ratios in the 4520 - 4540 \AA reference spectral band :

$E_A(\lambda_0)/F_A(\lambda_0) = 0.44\%$ a value similar to S_A/S_\odot as seen from the Moon where Fiber A is located; this leads to $L_A = 569$ arcsec;

$E_B(\lambda_0)/F_B(\lambda_0) = 3.12\%$ a value similar to S_B/S_\odot as seen from the Moon where Fiber B is located; this leads to $L_B = 1\,063$ arcsec.

In conclusion, from all parameters fully known at a given observing time, Eq. 14 gives access to direct evaluations of $h(\lambda)$, either in arcsec seen from the Moon or in km above (or below) the Earth's reference limb at $h(\lambda_0)$.

The extracted values of $h(\lambda)$ are shown in Fig. 6, obtained when using the 20h44 UT eclipse observations compared to the 02h56 UT full Moon ones at about the same air mass and over the same regions on the Moon. The extracted altitudes are relative to the reference altitude $h(\lambda_0)$, here equal to 0. As expected, the evaluations can be either positive (higher altitudes) or negative (lower altitudes).

To check the validity of several of our assumptions we calculated the same $h(\lambda)$ function extracted again from the 20h44 UT eclipse observations compared to both full Moon observations, the one at 02h56 UT as well as the 00h12 UT one made at different air masses, BERV and over distant regions on the Moon (see Table 1). This allows us to check that our evaluations are not sensitive to air masses or BERV variations (see Fig. 7), because both extracted $h(\lambda)$ functions are very similar in all their details. Although nearly identical (non discernable at full spectral resolution as in Fig. 6), the result indicates however that some broad band variation is present. It is not caused by an improper air mass correction because the produced effect cancels in two spectral regions: the first one at $4\,530\text{ \AA}$ (by definition, since this is our reference wavelength) and again around $6\,300\text{ \AA}$. That the observed relative variation of the transmission remains small in the blue and more important in the red is indeed in contradiction with an air mass correction, which has to be stronger in the blue (see Fig. 2). We thus conclude that the observed relative variation is more probably due to lunar albedo changes over different lunar regions.

This broadband effect could however be the cause of additional systematic errors in the altitude evaluations.

4.4. Error estimation

A simple visual analysis of Figs. 6 and 7 gives some idea of the errors estimated for the $h(\lambda)$ evaluations. First in Fig. 6, the error due to the photon noise in the observations is $\sim \pm 1$ km for all data points shown but clearly increases toward shorter wavelengths (below $5\,000\text{ \AA}$) due to the decreasing sensitivity of the instrument toward these wavelengths. Furthermore in this spectral region the impact of the improper order corrections is more and more important as more easily visible in Fig. 7. This effect induces an additional systematic error below $5\,000\text{ \AA}$ (of $\sim \pm 2.5$ km) and above $6\,400\text{ \AA}$ (of $\sim \pm 1$ km). Finally, although not all possible lunar terrains were sampled, we can guess from the different regions observed that an additional systematic error due to lunar albedo variations could be on the order of $\sim \pm 1$ km. This means that for our first attempt to estimate the Earth $h(\lambda)$ function we cannot produce absolute altitudes to better than approximately $\sim \pm 2.5$ km.

5. Discussion

5.1. Model calculation

The information extracted from the presented spectra is $h(\lambda)$, thus we are exactly in the situation of an extrasolar planetary transit. In effect, a spectrum recorded during a transit is *not* the spectrum of the absorbing species, but only the spectral signatures (in terms of altitude) of the *highest* absorbing species within the observed atmosphere. For instance, in the central region of the spectrum (Fig. 6) the main feature is the Chappuis band of ozone, corresponding to altitudes known to be in the 30 km range, other detectable species are only those able to efficiently absorb above. As we will see, oxygen and sodium are also detected with the present observations, but not H_2O .

In order to properly interpret our observations, we have to use model calculations to estimate the altitude at which the Earth atmosphere becomes transparent, as a function of wavelength and for a grazing line of sight exactly as in a transit situation.

Standard Earth atmospheric model calculations are from *e.g.* Ehrenreich et al. (2006) or Kaltenegger & Traub (2009). From these model calculations, one can evaluate the effective Earth radius at each wavelength, and from it, the effective height of the Earth atmosphere as a function of wavelength. From Fig. 3 of Kaltenegger & Traub (2009), the effective altitude corresponding to the tip of the Chappuis band absorption (near $6\,000\text{ \AA}$), is on the order of 30 km, revealing that the atmosphere becomes nearly opaque below this altitude at this wavelength.

In our model calculation we used an unidimensional single scattering transmission model based on the model described by Ehrenreich et al. (2006) to obtain the theoretical transmission spectrum of the terrestrial atmosphere. The pressure, temperature, and mixing ratio profiles of the considered atmospheric components are shown in Fig. 8 and come from the US Standard Atmosphere 1976 spring-fall pressure-temperature profile (COSEA 1976; Cox 2000). For simplicity, we chose to only include molecular nitrogen (N_2), molecular oxygen (O_2), and ozone (O_3) in the model. Molecular nitrogen contributes to the transmission spectrum via the Rayleigh-scattering of light. The Rayleigh-scattering cross section of N_2 depends on the N_2 refractive index, which is calculated according to Snee & Ubachs (2005). Within the SOPHIE spectral range, molecular oxygen contributes to the transmission spectrum through i) photoabsorptions by the forbidden $^1\Sigma_g^+ - ^3\Sigma_g^-$ transition bands B (1–0) at $6\,880\text{ \AA}$ and γ (2–0) at $6\,280\text{ \AA}$, and ii) through Rayleigh scattering. The line parameters for the O_2 bands are extracted from the HITRAN 2008 molecular spectroscopic database (Rothman et al. 2009), scaled to the atmospheric temperature and pressure profiles used, and convolved with a Gaussian profile with full-width at half-maximum matching the spectrograph resolution. The Rayleigh-scattering cross sections of O_2 are calculated following Snee & Ubachs (2005) using refractive indices from Bates (1984). We retrieved the UV/visible photoabsorption cross section of O_3 at 293 K and 1 bar from the GEISA 1997 data base (Jacquinot-Husson et al. 1999).

We recall here that we are not doing a fit of our data but just compute altitude signatures related to a “standard” Earth atmospheric model.

5.2. Broadband signatures

The variable effective altitude h (as a function of wavelength) is shown on Fig. 9 for both model calculations and as extracted from the observations, the overall contribution of O_3 , O_2 and

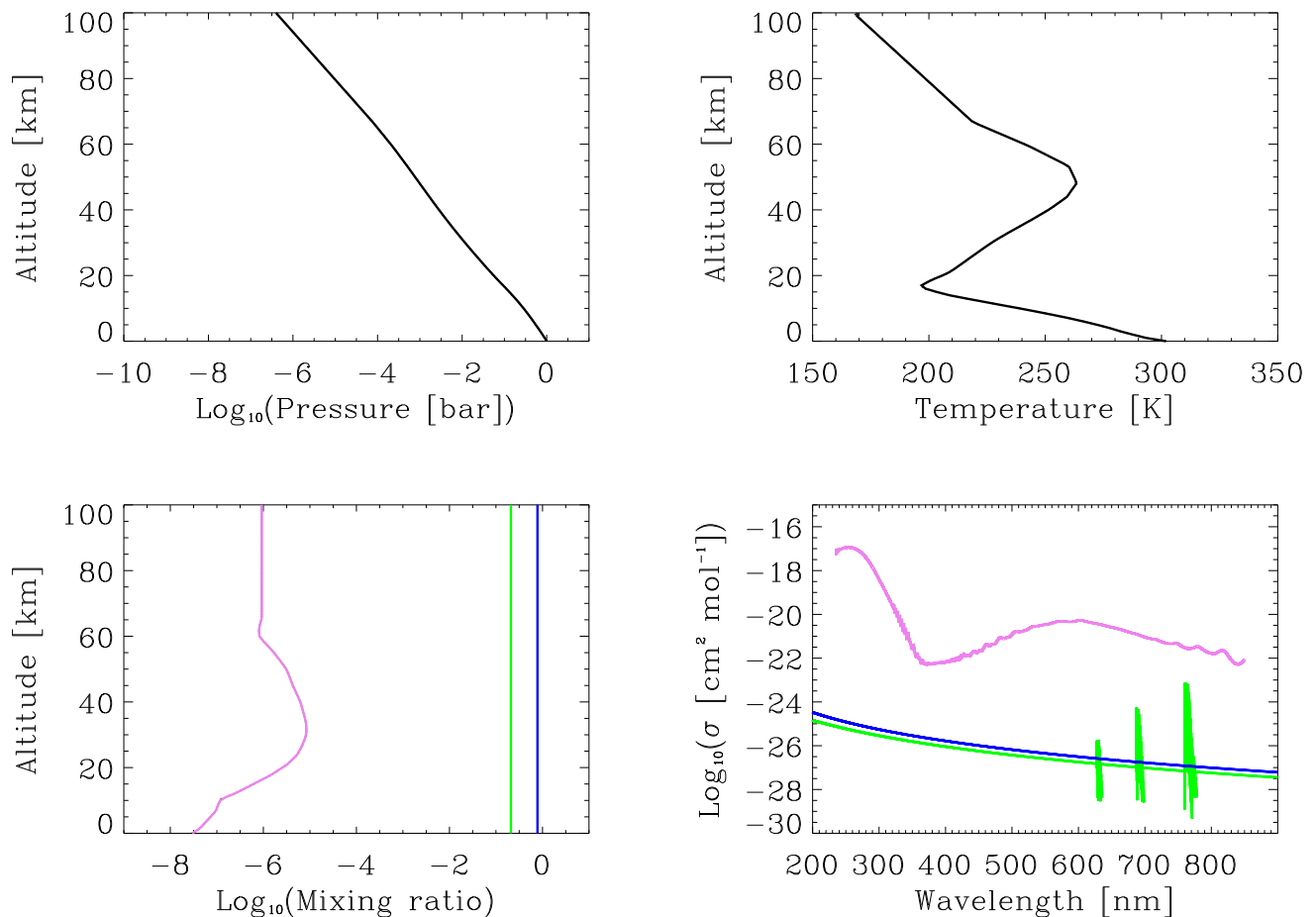


Figure 8. “Standard” atmosphere used in the model calculation (see text) : **Upper left** the pressure profile, **upper right** the temperature profile, **lower left** the N_2 (blue), O_2 (green) and O_3 (pink) mixing ratio as a function of altitude (km) and **lower right** the N_2 (blue) Rayleigh, O_2 (green) Rayleigh and molecular bands and O_3 (pink) cross sections as a function of wavelength (in nm).

Rayleigh scattering due to both N_2 and O_2 , along with the Rayleigh contribution alone are also shown.

In the selected reference domain from 4 520 to 4 540 Å, the model calculation predicts an altitude equal to 23.8 km. Because our observational evaluation of h is *relative* to the altitude in the reference domain, we shift our *relative* $h(\lambda)$ evaluations by +23.8 km to be comparable to the model calculation. Since furthermore our reference domain falls at the tip of a SOPHIE echelle order fluctuation, we corrected by an additional systematic shift of about 1.5 km (half of the echelle fluctuation). The model and observations are shown in Fig. 9, where a 25.3 km reference altitude is used in the 4 520 to 4 540 Å reference domain range.

Our observed evaluations as shown in Fig. 9 are binned over 200 pixels (~ 2 Å) to better underline the observed broadband variations. It can be seen that the errors over the broadband signatures are mainly due to systematic errors, as opposed to photon noise, and are on the order of the SOPHIE approximate order correction, *i.e.* $\sim \pm 2.5$ km.

The comparison between the observed variations and model calculations is very satisfactory. Even the observed ozone distribution seems probably less extended in altitude than the standard model by about 2 km, a very plausible situation because ozone variations are known to exist around the Earth in terms of both

location and epoch (Millier et al. 1979, Thomason & Taha 2003, Borchì & Pommereau 2007). There is no reason that the selected standard atmospheric model exactly corresponds to the Earth atmospheric conditions at the precise location over the observed Earth’s limb.

5.3. Narrowband spectral signatures

The acute need for high spectral resolution is highlighted by the detection of other species, which are producing signatures at altitudes above the ozone level.

5.3.1. Sodium detection

The spectral region containing the NaI doublet is shown in Fig. 10. To repeat the discussion presented in Sect. 3, concerning the zero flux level correction, the result without any correction applied is also shown. Obviously, the atmospheric NaI doublet does not show up without that correction, and furthermore the broad wings of the two NaI solar lines are still present while our extraction process should have entirely washed out any solar line signature, as it is indeed almost perfectly the case in Figs. 6 or 9.

This correction introduces an additional systematic error, which produces an altitude shift of about 1.5 km per 0.0001 step

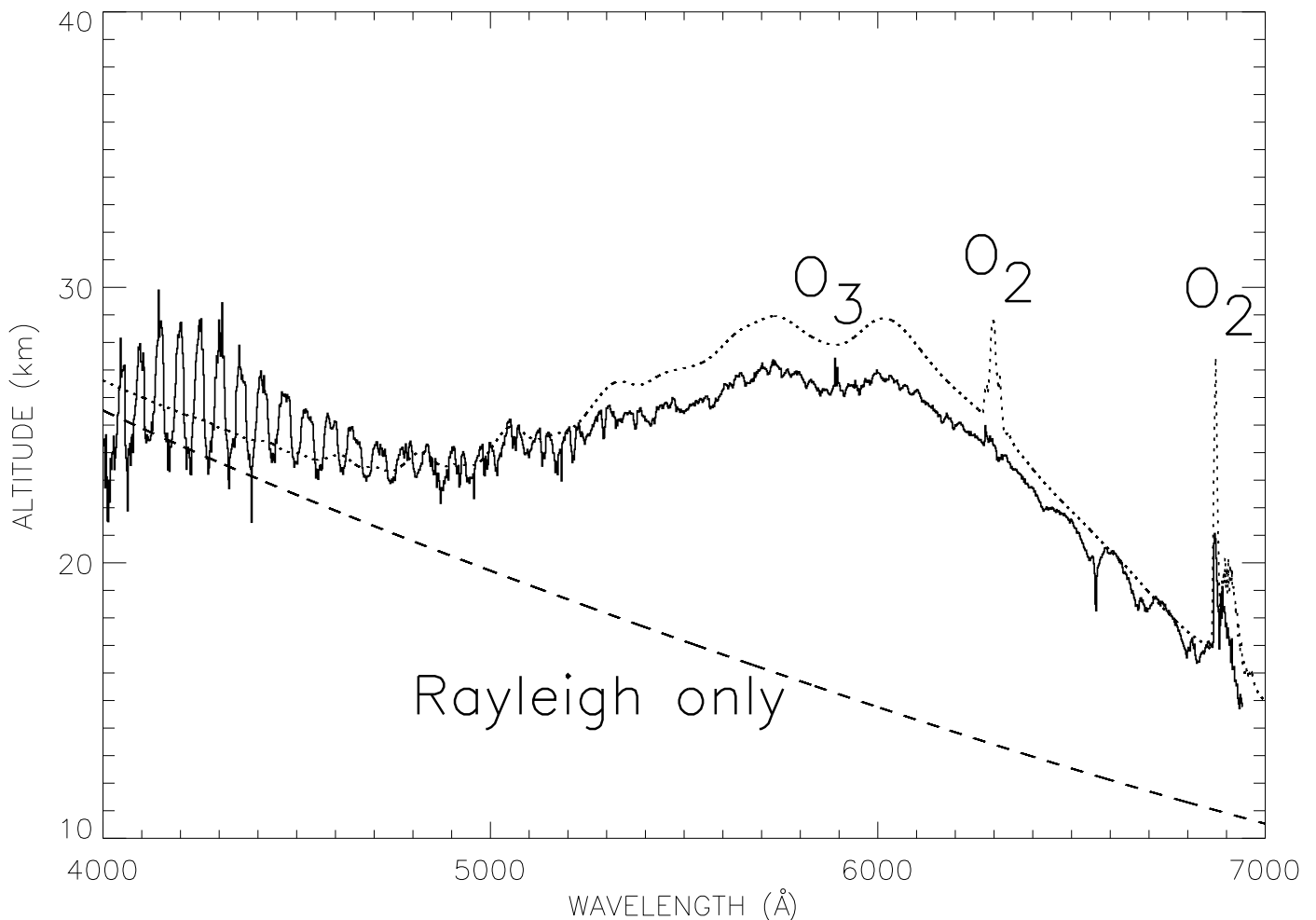


Figure 9. Observed binned variations (solid line) of the effective altitude h compared to model calculations (also binned). The Rayleigh-alone model calculation is shown (dashed line) along with the complete atmospheric model calculation (dotted line), which includes N_2 , O_2 and O_3 (see text).

change in the zero level (see Fig. 10). This is small compared to the systematic error due to the instrumental order correction (on the order of ± 2.5 km), which thus remains the major cause of uncertainty on our extracted altitude level.

Note here a very interesting point. We know that both H_2O and O_2 produce strong absorption signatures in the Earth atmosphere and, as shown in Fig. 2, they have relatively similar signatures near 5900 \AA (in the NaI lines vicinity) for H_2O or around 6300 \AA for O_2 . We will see in the sections below that O_2 is indeed easily detected in the grazing (transit like) observations of the atmosphere, while we see here that none of the numerous H_2O lines present in that spectral range (see Fig. 3) are detected. The reason is very simple: H_2O is hidden in the transit like observations because it is at lower altitudes than ozone, while O_2 , a major constituent of the atmosphere, is still present in sufficient quantities at higher altitudes, and indeed shows up above the ozone layer. This is exactly what models do predict (see *e.g.* Kaltenecker & Traub 2009) and thus reveals the quality and consistency of our analysis, from which only species thought to show up are indeed detected.

The zero level correction induces additional very large errors on the estimated altitude of the NaI spikes: the NaI 5890 \AA line peaks up from 35 to 100 km, while the 5896 \AA one from 35 to 65 km altitudes.

NaI is known to be present in the Earth atmosphere within a layer at about 92 km, presenting an average thickness of about 11 km (Moussaoui et al. 2010). If it was completely opaque in the two NaI lines, we should have found the same level in both lines at lower altitudes than the 92 km, depending on the ratio between the atmospheric line width ($\sim 0.03 \text{ \AA}$) and the instrument spectral resolution ($\sim 0.09 \text{ \AA}$). This should lead to reduced altitudes of about one third of 92 km above the 30 km ozone signature, *i.e.* ~ 50 km.

This could correspond to our 0.0002 zero level correction, leading to both line levels at about 35 km altitude, a little low when compared to our evaluation.

However, we can also directly evaluate the line’s opacity in the 92 km altitude layer by using the observed average vertical sodium column density of the layer to be on the order of 4.10^{13} m^{-2} (Moussaoui et al. 2010). Using the average altitude, thickness, and “vertical” column density of the layer, we can translate these numbers into an average “horizontal” column density at 92 km of altitude and found it to be on the order of $3.10^{11} \text{ cm}^{-2}$, leading to an optical thickness in the core of the line on the order of 3 in the strongest NaI line and 1.5 in the weaker one. Both lines are thus opaque, but not strongly opaque. The known variability of the NaI layer could be the reason for this slightly less opacity, which renders it probable that

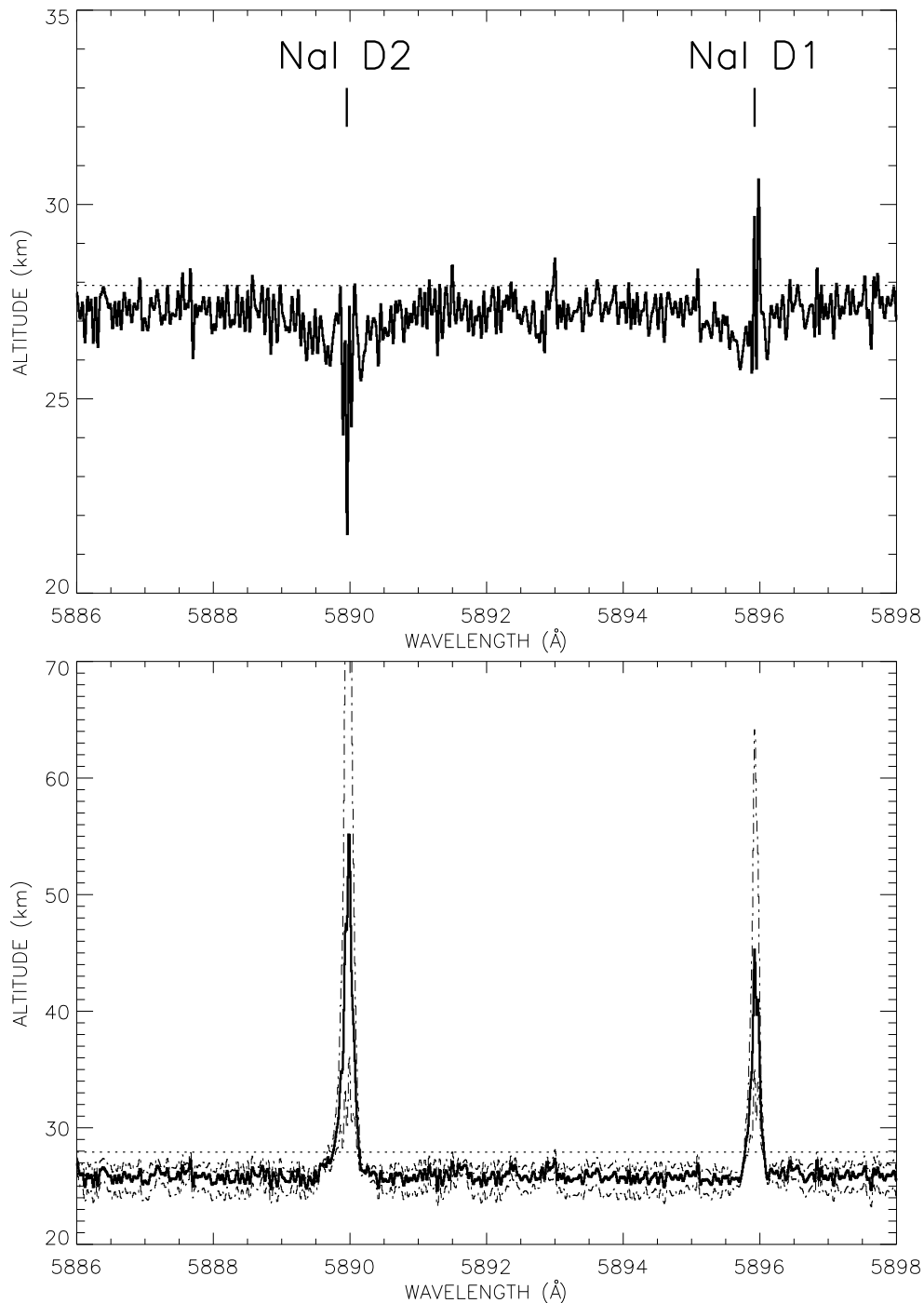


Figure 10. NaI doublet spectral region. The shifted $h(\lambda)$ variations (solid lines) are shown along with the level of the model ozone prediction (dotted line). **Upper plot.** The zero level correction as detailed in Sect. 3 is not applied. The two NaI narrow atmospheric signatures do not show up while through our complete data analysis method the broad wings of the sodium solar lines are obviously still present, contrary to expectation (the solar broad lines wings should not appear in any information uniquely related to the Earth atmosphere). **Lower plot.** The zero level correction by subtracting a 0.0003 value is now applied (see text). The NaI solar wings have disappeared, while the narrow NaI atmospheric signatures clearly show up. To show the impact of the zero level correction, the two evaluations corresponding to the 0.0002 and 0.0004 zero corrections are overplotted (thin dash-dotted lines). This gives a direct idea of the induced error bars on our evaluation.

a marginally opaque layer was observed during the eclipse, then leading to two different altitudes for the observed doublet spikes corresponding to the also plausible values as the ones observed with our 0.0003 zero corrections, which are at 55 and 45 km respectively.

From this brief quantitative discussion, we note that the 0.0004 zero correction is certainly a limit because, in that case, the altitude of the strongest line is at more than 100 km, *i.e.* too high, even above the altitude of the layer itself.

The NaI atmospheric detection is certainly compatible with what is known about the Earth layer, both qualitatively and quan-

tatively. This shows that our high-resolution approach could give us access to narrow line signatures, and thus gives us confidence in searching for other species. We detail this search in the following sections.

5.3.2. The 6 880 Å oxygen molecular band

Two molecular oxygen absorption bands have their signatures in the observed spectral range. We used for them the same zero level correction as for the NaI lines.

The strongest one, the O₂ forbidden $^1\Sigma_g^+ - ^3\Sigma_g^-$ transition band B (1–0) at 6 880 Å, is shown in Fig. 11. All molecular band peaks are clearly present, undoubtedly signing the O₂ detection. To evaluate the impact of the zero level adjustment, the three evaluations of $h(\lambda)$ made with the three values, 0.0003 ± 0.0001 , are also shown in Fig. 11. This directly shows that in this spectral range, the zero level adjustment adds a systematic error of about $\sim \pm 2.5$ km in the continuum and up to $\sim \pm 10$ km in the peaks, showing that their absolute estimates from these observations are quite imprecise.

However, the average peak altitude and its relative height variations are certainly more meaningful. In particular, the average height of the 0.0004 correction produces signatures closer to the model predictions, suggesting that the zero level correction may be slightly wavelength-dependant or that its acceptable range is reduced to 0.00035 ± 0.00005 . One can also note that the observed peak heights when moving redward seem to drop more rapidly than in the model prediction, an obvious indication of a cooler atmosphere than the “standard” one selected for the model calculation. This suggests that better adjusted Earth atmospheric model parameters in terms of vertical temperature-pressure profile are needed. This is however beyond the scope of this paper, in which we just intend to show that some species detection is feasible according to that observational approach in both qualitative and quantitative terms. The fine adjustment of model parameters will be done in future papers according to future observations to be made, all along a complete lunar eclipse to search for Earth atmospheric variations along the Earth limb sampled during the eclipse evolution.

5.3.3. The 6 280 Å oxygen molecular band

The other oxygen molecular band in the observed spectral range is the γ (2–0) at 6 280 Å. It is shown in Fig. 12, for which the same zero level corrections have again been used.

The narrow spike positions of the band are clearly detected. This band is weaker however and emerges only by ~ 1 km above the continuum. A detailed discussion of this weaker signature is again beyond the scope of this paper, but this second detection of O₂ demonstrates the quality and precision of our approach, which allows us to detect atmospheric signatures just beyond the photon noise. Indeed the photon noise induces in that region of high solar flux and high instrument sensitivity only a ± 0.5 km uncertainty over our altitude evaluation.

Note that for this O₂ molecular band we have checked the perfect match of the peak’s spectral positions with the predicted ones while it seems that again their heights drop faster than the peak’s altitude variations evaluated in the model calculation. This appears to confirm that the “standard” atmospheric model selected for that comparison is probably hotter than the observed atmosphere, particularly in the sampled ~ 30 km altitude range. If this were true it may also explain the slight mismatch found between the predicted and the observed O₃ Chappuis band (see

Fig. 9), in which the model is higher by ~ 2 km. This band will certainly be scaled down by some amount in a lower temperature model, simply because the atmospheric scale height will be reduced.

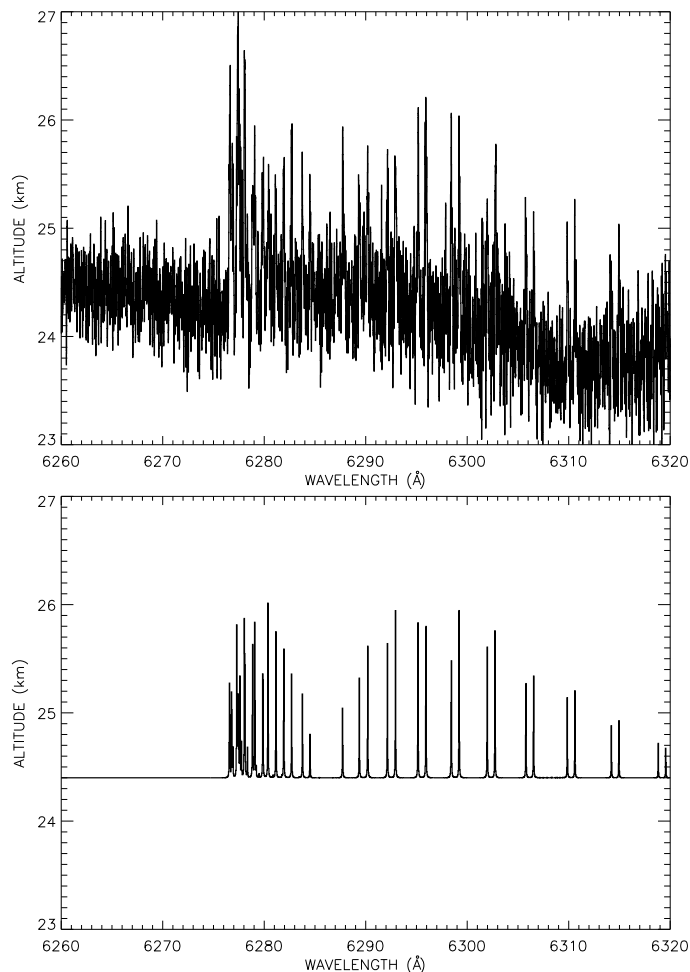


Figure 12. γ (2–0) 6 280 Å O₂ molecular band. **Upper plot.** Same background correction as in Fig. 10 (see text). The solid line represents the altitude information as extracted from the SOPHIE data set. **Lower plot.** The O₂ band spectral structure is shown to demonstrate the clear coincidence in position of the repeated spikes signing the O₂ detection.

5.4. Previous lunar eclipse studies

Other observations of the 2008 August 16 lunar eclipse were completed through inter-calibrated optical and near-infrared ground-based observations at the William Herschel and Nordic Optical Telescopes by Pallé et al. (2009), to provide continuous wavelength coverage from 0.36 to 2.40 μm . Their approach was very similar to ours, except that their spectral resolution is somewhat lower ($\sim 1\,000$ instead of $\sim 75\,000$). They also focused on umbral, penumbral, and out-of-the-eclipse observations without detailing (as we did) the precise location within the penumbra from where the observations were made. This is important because it leads toward only qualitative detections instead of quantitative ones.

Furthermore, the Pallé et al. (2009) transmission spectrum is “calculated by computing the ratio of the umbra/penumbra

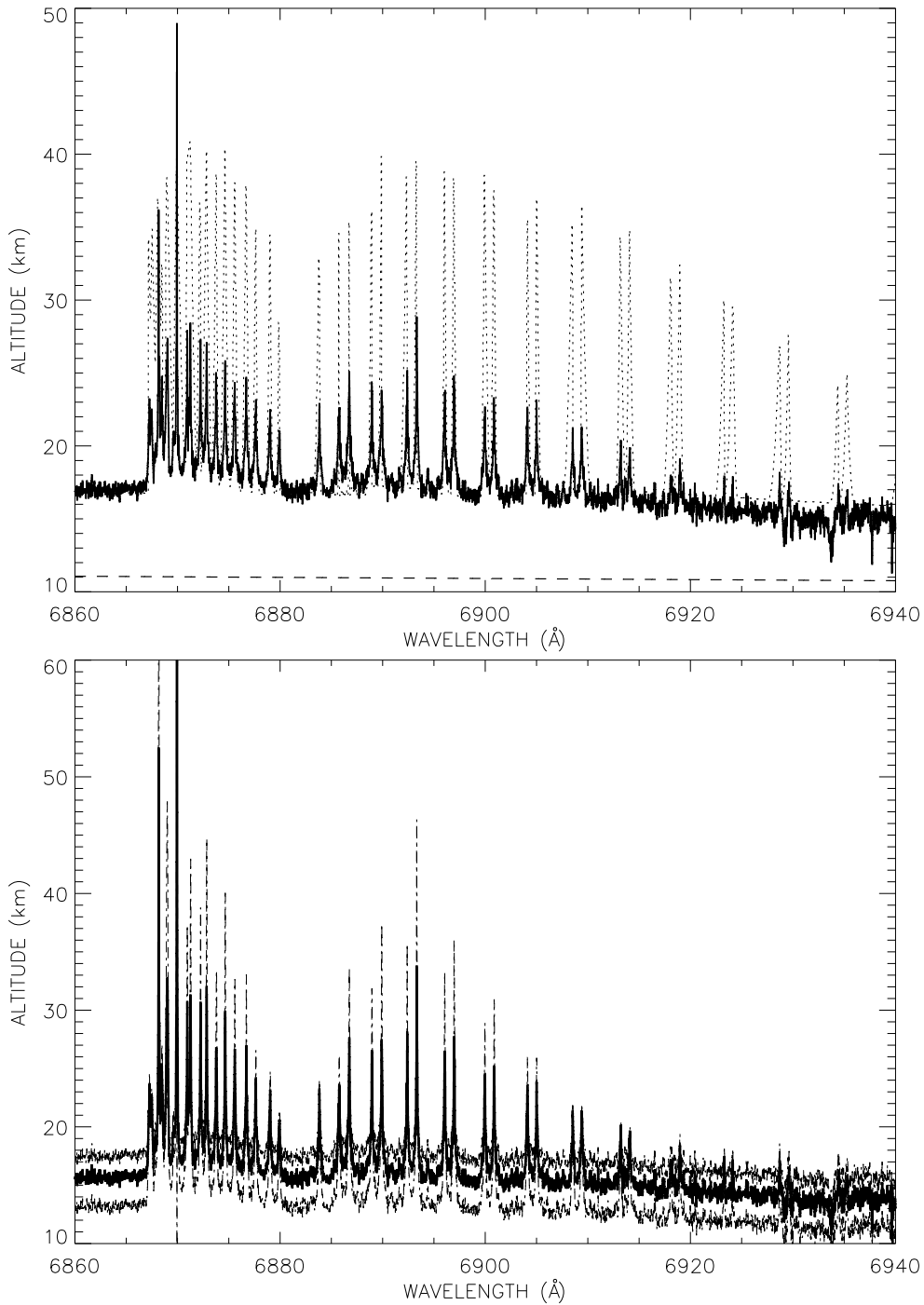


Figure 11. O_2 forbidden $^1\Sigma_g^+ - ^3\Sigma_g^-$ transition band B (1-0) at 6880 Å. The same background correction as in Fig. 10 has been applied (see text). **Upper plot.** The solid line represents the altitude information extracted from the *SOPHIE* data, while the dotted line is the model calculation, in which O_2 absorption is included from 6856 Å upwards. The narrow atmospheric signatures due to the O_2 absorption are clearly seen. The sharp peaks perfectly match the model with respect to spectral positions, while their heights could be quite different. **Lower plot.** The thick solid line again represents the evaluated altitude for the 0.0003 zero level correction, while the thin dash-dotted lines show the extreme possible variations of the estimated levels due to the 0.0002 (lower evaluations in the peaks and higher ones in the continuum) and 0.0004 (higher evaluations in the peaks and lower ones in the continuum) zero level corrections.

regions taken at the same averaged air mass in order to minimize the local atmospheres telluric line variations”. This means that the observed transmission spectrum they evaluated is not the transit-like spectrum of the Earth. Indeed the umbra spectra resulting uniquely from rays deflected by the lower and dense layers of the atmosphere are unobservable during a real transit

of an extrasolar planet since the corresponding stellar light deflected through the lower layers of the atmosphere moves away from the observer line of sight. What Pallé et al. (2009) have reported are identifications of different atmospheric specie signatures only present in the lower parts of the atmosphere as seen

within the umbra, but not the real transit signatures, which are only observable within the penumbra, as we did.

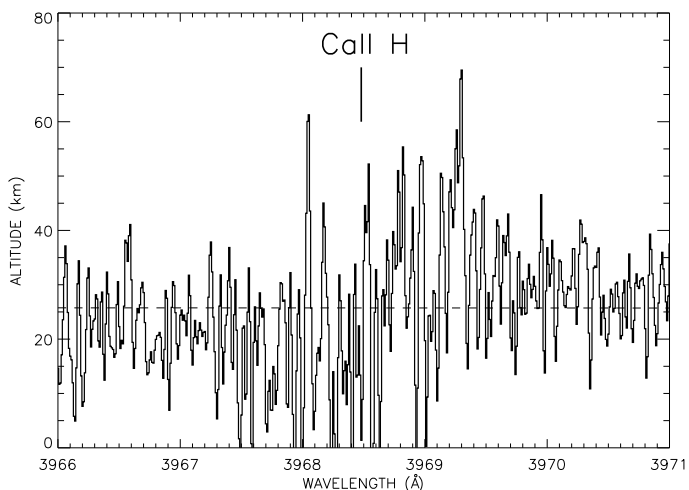


Figure 13. The $h(\lambda)$ variation as extracted from the region of the CaII H line. Because the S/N is quite poor in that region the photon noise in this part of the spectrum is more than 10 times higher than in the other spectral regions. Large signatures similar to the NaI ones should be visible however, but according to the low CaII content of the Earth atmosphere, they are simply not observable, as it is the case here.

In particular, Pallé et al. (2009) have not detected the NaI signatures. They are produced at very high altitudes only (~ 92 km) and should be indeed unobservable in the lunar umbra. They mention the detection of CaII signatures however, while it is also known that in the Earth atmosphere CaII ions are only present at high altitudes (Granier et al. 1989). CaII is furthermore about 120 times fainter than NaI, thus the CaII detection (and not the NaI one) is quite a surprise. Because we have in our hands much lower S/N SOPHIE observations at our disposal, we tried however to look for possible CaII signatures. As shown in Fig. 13, nothing shows up. We conclude that the Pallé et al. (2009) CaII detection is probably an artifact.

To enforce that argument we note that Pallé et al. (2009) clearly detected H₂O signatures (a low altitude species) at ~ 7200 Å, while as shown from model predictions (Kaltenegger & Traub 2009), these could not show up in a transit spectrum being hidden below the O₃ and Rayleigh signatures (see Fig. 9). This is why the different H₂O signatures we have seen in our observation of the “vertical” Earth atmosphere (see Fig. 2) do not show up in any of our “horizontal” transit-like signatures within the Earth atmosphere, because they are simply too low in altitude as predicted from the model calculations (see *e.g.* Fig. 10 where several H₂O lines should have shown up around the NaI doublet, if present).

The Pallé et al. (2009) study in a larger spectral domain than ours reveals the great variety of detectable species, while ours reveals how precisely the atmospheric content could be analyzed.

5.5. Detection of O₂ and O₃ in an extrasolar planet atmosphere during transits

The purpose of this work is also to show and evaluate the feasibility of the detection of O₂ and O₃ in the atmosphere of an Earth-like extrasolar planet during transits.

We will not repeat the arguments of Lecavelier des Etangs & Ehrenreich (2005) here but only recall the extreme difficulty of these observations, which demand $10^{-6} - 10^{-8}$ accuracy to be obtained over the observed stellar flux before, during, and after the planetary transit. This is a real challenge even merely in terms of photon noise, and asks for very large telescopes in the 10 to 30 m diameter range. This is only possible from the ground in a relatively short-term perspective, in particular in the frame of the *ELTs* (Extremely Large Telescopes) concepts that are planned to operate during the coming decade.

The *ELTs* are however observing through the Earth atmosphere, and it is difficult to argue that such high precision accuracies will be achieved.

Our observations show that although the O₃ Chappuis band seems to be easier to detect according to the broad spectral range over which it extends, it is still possible to think that uncontrolled systematics due to atmospheric fluctuations will perturb the detection. This is the obvious difficulty of broadband detections.

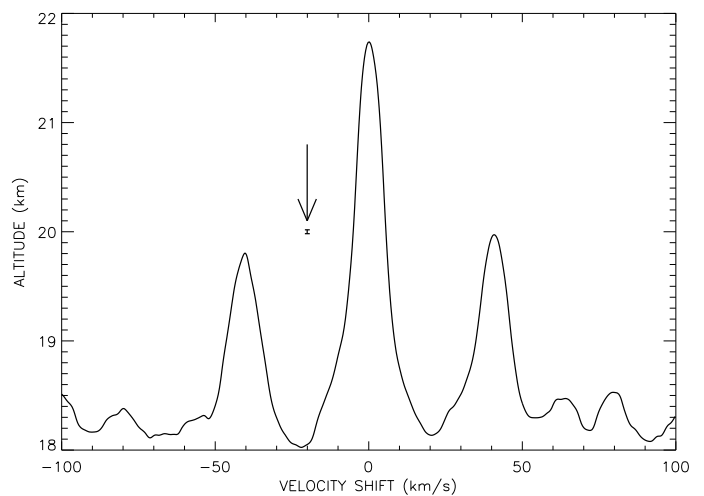


Figure 14. Correlation function extracted from the O₂ forbidden $1\Sigma_g^+ - 3\Sigma_g^-$ transition band B (1–0) at 6880 Å by using a mask centered on each of the spike positions over a ± 0.1 Å width. The typical error bar of this function is indicated (arrow) and is on the order of the tracing thickness, according to the total spectral width sampled by the mask.

On the other hand, our O₂ observation via high-resolution spectroscopy signatures is very promising because it can be shown that the addition of all spectral lines over only the O₂ forbidden $1\Sigma_g^+ - 3\Sigma_g^-$ transition band B (1–0) at 6880 Å is equivalent to a detection over a ~ 8 Å band pass. This places the O₂ detection among the feasible ones from the ground with *ELT* telescopes at least in terms of photon fluxes. But the use of high spectral resolution and stable spectrographs, similar to the one presently used for radial velocity searches of extrasolar planets, has proved to be possible in a quite difficult case, which is to observe the Earth’s atmosphere as a transiting planet through the Earth atmosphere itself, *i.e.* all searched for and perturbing spectral signatures are exactly at the same wavelengths. For transiting extrasolar planets the situation will be more favorable because a simple shift of ~ 10 to 30 km/s or more will be enough to clearly separate them as shown through the correlation function extracted with an O₂ like mask (see Fig. 14). This should be a relatively common observational situation. Note the secondary peaks of the correlation function which are due to the rel-

atively regular separation between the successive O₂ line peaks. Because these are however well separated, this should not prevent O₂ detection over this molecular band.

Our observation shows that with high spectral resolution, systematics are much easier to control because extremely nearby spectral regions behave similarly to each other in terms of any systematic effects. This may be one of the very few possible approaches to reach this goal, which is detecting O₂, one of the strongest signatures of life bearing atmospheres.

Observing O₂ and O₃ species in extrasolar Earth like planetary atmospheres, both accessible from the ground in the same spectral range, shows that these searches will be attainable for *ELT* observatories equipped with high spectral resolution and high stability spectrographs.

6. Conclusion

We have shown that Lunar eclipse spectral observations are able to reveal the atmospheric content of the Earth's atmosphere, in particular, broadband signatures of O₃ and Rayleigh scattering as well as narrowband features of NaI and O₂ observed at high spectral resolution. As these observations mimic future studies of transiting extrasolar planets, we are confident that quantitative information about extrasolar atmospheres will be within reach. Furthermore, both Rayleigh scattering and O₃ are broadband and extend across the visible part of the spectrum, just where solar-like stars have their maximum flux, making it easier to obtain the high signal-to-noise values necessary for a positive exoplanet detection.

More studies of Lunar eclipses should be completed in order to better quantify the present detections and more precisely show the feasibility of future extrasolar Earth-like planets studies. These studies, with extremely large ground-based telescopes, should allow at least the detections of ozone and O₂. In any case, these observations will be extremely difficult because the required accuracy is in the 10⁻⁶ to 10⁻⁸ range. This is why observing in the visible range, where orders of magnitude more photons are available, could ultimately be one of the most promising approaches.

Acknowledgements. The authors thank the staff of Haute-Provence Observatory for their contribution to the success of the *SOPHIE* project and their support at the 1.93-m telescope. We thank the "Programme National de Planétologie" (PNP) of CNRS/INSU, the Swiss National Science Foundation, and the French National Research Agency (ANR-08-JCJC-0102-01 and ANR-NT05-4-44463) for their continuous support of our planet-search programs.

We also thank W.A. Traub, our referee, for mentioning the ring effect that possibly explains the zero shift correction and E. Pallé for very constructive discussions before the observing campaigns of the 2008 August 16 Moon eclipse.

DE acknowledges financial support from the Centre National d'Etudes Spatiales (CNES) and NCS the support from the European Research Council/European Community under the FP7 through a Starting Grant, as well as from the Fundação para a Ciência e a Tecnologia (FCT), Portugal, through a Ciência 2007 contract funded by FCT/MCTES (Portugal) and POPH/FSE (EC), and in the form of grants reference PTDC/CTE-AST/66643/2006 and PTDC/CTE-AST/098528/2008.

References

- Arnold, L., Gillet, S., Lardièrre, O., Riaud, P., & Schneider, J. 2002, *A&A* 392, 231
- Arnold, L. 2008, *Space Science Reviews*, 135, 323
- Ballester, G.E., Sing, D.K., & Herber, F. 2007, *Nature* 445, 511
- Barman, T. 2007, *ApJ* 661, L191
- Bates, D.R. 1984, *P&SS*, 32, 785
- Bird, R.E., Hulstrom, R.L., Kliman, A.W., & Elderling, H.G. 1982, *Applied Optics* 21, 1430
- Borchi, F., & Pommereau, J.-P. 2007, *Atmos. Chem. Phys.* 7, 2671
- Bordé, P., Rouan, D., & Léger, A. 2003, *A&A*, 405, 1137
- Bouchy, F., Hébrard, G., Udry, S., et al. 2009, *A&A*, 505, 853
- Charbonneau, D., Brown, T.M., Noyes, R.W., & Gilliland, R.L. 2002, *ApJ* 568, 377
- COESA (Committee on Extension to the Standard Atmosphere), U.S. Standard Atmosphere 1976 (Washington DC: Government Printing Office)
- Cox, A.N. 2000, *Allen's Astrophysical Quantities* (4th ed.; New York: AIP)
- Danjon, A. 1936, *Annales de l'Observatoire de Strasbourg* 3, 139
- Désert, J.-M., Vidal-Madjar, A., Lecavelier Des Etangs, A., Sing, D., Ehrenreich, D., Hébrard, G. & Ferlet, R. 2008, *A&A* 492, 585
- Désert, J.-M., Lecavelier des Etangs, A., Hébrard, G., Sing, D.K., Ehrenreich, D., Ferlet, R., & Vidal-Madjar, A. 2009, *ApJ* 699, 478
- Ehrenreich, D., Tinetti, G., Lecavelier Des Etangs, A., Vidal-Madjar, A., & Selsis, F. 2006, *A&A* 448, 379
- Ehrenreich, D., Hébrard, G., Lecavelier des Etangs, A., Sing, D.K., Désert, J.-M., Bouchy, F., Ferlet, R., & Vidal-Madjar, A. 2007, *ApJ* 668, L179
- Fortney, J. J. and Marley, M. S. and Lodders, K. and Saumon, D. and Freedman, R. 2007, *ApJ*, 627, L69
- Gedzelman, S. D., & Vollmer, M. 2008, *Applied Optics* 47, 149
- Granier, C., Jegou, J.P., & Mégie, G. 1989, *Journal of Geophys. Res.* 94, 9917
- Hayes, D.S., & Latham, D.W. 1975, *ApJ* 197, 593
- Hernitschek, N., Schmidt, E. & Vollmer, M. 2008, *Applied Optics* 47, 62
- Jacquinet-Husson, N., Arié, E., Ballard, J., et al. 1999, *JQSRT* 62, 205
- Kaltenegger, L., & Traub, W.A. 2009, *ApJ* 698, 519
- Lecavelier des Etangs, A., & Ehrenreich, D. 2005, 39th ESLAB Symposium on Trends in Space Science and Cosmic Vision 2020, Edt. F. Favata, J. Sanz-Forcada, A. Giménez, and B. Battrock. ESA SP-588, 73
- Lecavelier Des Etangs, A., Pont, F., Vidal-Madjar, A., & Sing, D. 2008a, *A&A* 481, L83
- Lecavelier Des Etangs, A., Vidal-Madjar, A., Désert, J.-M., & Sing, D. 2008b, *A&A* 485, L865
- Léger, A., Selsis, F., Sotin, C., et al. 2004, *Icarus* 169, 499
- Léger, A., Rouan, D., Schneider, J., et al. 2009, *A&A* 506, 287
- Millier, F., Vidal-Madjar, A., Guidon, J., & Roble, R.G. 1979, *Geophys. Res. Lett.* 6, 863
- Moussaoui, N., Clemesha, B.R., Holzlohner, R., Moussaoui, Simonich, D.M., Bonaccini Calia, D., Hackenberg, W., & Batista, P.P. 2010, *A&A* 511, A31
- Pallé, E., Osorio, M.R.Z., Barrena, R., Montañés-Rodríguez, P., & Martn, E.L. 2009, *Nature* 459(7248), 814
- Perruchot, S., Kohler, D., Bouchy, F., et al. 2008, in *Ground-based and Airborne Instrumentation for Astronomy II*. Edited by McLean, Ian S. & Casali, Mark M., Proceedings of the SPIE, Volume 7014, pp. 70140J-12
- Queloz, D., Bouchy, F., Moutou, C., et al. 2009, *A&A* 506, 303
- Rothman, L.S., Gordon, I.E., Barbe, A., et al. 2009, *JQSRT* 110, 533
- Rouan et al. 2009, *CoRoT International Symposium I*, Paris, 2-5 feb. 2009
- Sagan, C., Thompson, W. R., Carlson, R., Gurnett, D., & Hord, C. 1993, *Nature*, 365, 715
- Sing, D.K., Vidal-Madjar, A., Désert, J.-M., Lecavelier des Etangs, A., & Ballester, G. 2008a, *ApJ* 686, 658
- Sing, D.K., Vidal-Madjar, A., Lecavelier des Etangs, A., Désert, J.-M., Ballester, G.E., & Ehrenreich, D. 2008b, *ApJ* 686, 667
- Sing, D.K., Désert, J.-M., Lecavelier Des Etangs, A., Ballester, G.E., Vidal-Madjar, A., Parmentier, V., Hébrard, G., & Henry, G.W. 2009, *A&A* 505, 891
- Sneep, M., & Ubachs, W. 2005, *JQSRT* 92, 293
- Thomason, L.W., & Taha, G. 2003, *Geophys. Res. Lett.* 30, 1631
- Vidal-Madjar, A., Laurent, C., Bruston, P., & Audouze, J. 1978, *ApJ* 223, 589
- Vidal-Madjar, A., Lecavelier des Etangs, A., Désert, J.-M., Ballester, G.E., Ferlet, R., Hébrard, G., & Mayor, M. 2003, *Nature* 422, 143
- Vidal-Madjar, A., Désert, J.-M., Lecavelier des Etangs, A., Hébrard, G., Ballester, G.E., Ehrenreich, D., Ferlet, R., McConnell, J.C., Mayor, M., & Parkinson, C.D. 2004, *ApJL* 604, L69
- Wolf N.J., Smith P.S., Traub W.A., & Jucks, K.W. 2002, *ApJ* 574, 430
<http://www.lpi.usra.edu/resources/mapcatalog/usgs/I703/150dpi.jpg>